Chemical Science

Accepted Manuscript

This article can be cited before page numbers have been issued, to do this please use: M. A. Ali, J. H. Kim, Y. Kim, Y. Nam, J. Oh, W. Jang and D. Kim, *Chem. Sci.*, 2026, DOI: 10.1039/D6SC00941G.

ROYAL SOCIETY OF CHEMISTRY

rsc.li/chemical-science

Redox- and Protonation-Driven Baird and Clar Aromaticity in Asymmetric Multicyclic Octaphyrins

View Article Online
DOI: 10.1039/D6SC00941G

Md Ashif Ali[a], Ji Heon Kim[b,c], Younghun Kim[a], Yunwoo Nam[a], Juwon Oh*[b,c], Woo-Dong Jang*[a] and Dongho Kim*[a]

Affiliations

[a]Department of Chemistry, Yonsei University, 50 Yonsei-ro, Seodaemun-gu, Seoul 03722, Korea

[b]Department of Chemistry and Green-Nano Material Research Center, Kyungpook National University, Daegu 41566, Korea

[c]Department of Chemistry, Soonchunhyang University, Asan 31538, Korea

Email

JO: juwoh933@knu.ac.kr

WDJ: wdjang@yonsei.ac.kr

DK: dongho@yonsei.ac.kr

Abstract: Aromaticity tuning in octaphyrins provides a powerful platform for controlling redox behavior, spin states, and stimulus-induced structural reorganization in fully π-conjugated macrocycles. In contrast, asymmetric multicyclic systems incorporating fused, bridged architectures and heteroaromatic components remain largely unexplored. Herein, we describe the synthesis of a series of fully π-conjugated asymmetric multicyclic N-fused 36π octaphyrins incorporating bithiophene or benzithiophene units. These multicomponent systems undergo redox- and protonation-induced aromaticity switching with commensurate changes in their electronic- and spin-states. The neutral species are globally nonaromatic; protonation selectively drives one asymmetric octaphyrin into a rare triplet ground state stabilized by Baird aromaticity, whereas the other is stabilized by Clar sextet aromaticity, while two-electron oxidation induces global aromaticity in both systems. Comprehensive electronic and conformational analyses reveal that these multifaceted changes in aromaticity and spin

View Article Online
DOI: 10.1039/D6SC00941G

character originate from cooperative and competing π-electronic interactions between the constituent sub-macrocycles. These findings highlight fundamental design principles for modulating electronic and spin properties in fully conjugated multicyclic macrocycles through the controlled interplay of multiple π-electronic circuits.

Introduction: Aromaticity is a fundamental concept in organic chemistry that has long been used to understand the properties of π-conjugated materials. The unique energetic stabilization provided by cyclic delocalization of [4n+2] π electrons, as described by Hückel's rule,[1] plays a key role in shaping the physicochemical properties and reactivities of a wide range of organic molecules.[2] In polycyclic aromatic hydrocarbons (PAHs) composed of fused benzene rings, π-electrons are largely confined to individual phenylene units,[3] where the Clar sextet rule provides a qualitative tool for interpreting electronic structure and chemical behavior.[4-5] In contrast, the emergence of global (anti)aromaticity across the entire macrocyclic framework means that fully π-conjugated oligomeric macrocycles often display electronic characteristics that transcend the resonance effects of their monomeric units.[6-18] Moreover, in the excited state, aromatic stabilization and antiaromatic destabilization effects play a critical role as embodied in the concept of Baird aromaticity,[19-23] which predicts aromatic stabilization in the lowest triplet excited state.

Given the central role of aromaticity in molecular design, research has increasingly expanded into bridged octaphyrins (**1** and **2**),[24-25] molecular cages (**3**)[26] and fully π-conjugated multicyclic macrocycles (**4**)[27] (Chart 1). These systems are characterized by electronic coupling between their constituent sub-macrocycles and exhibit unique electronic structure and aromaticity effects. Depending on the system in question, the individual subunits can interact cooperatively, independently, or competitively. This allows for a formal fine-tuning of the redox potentials, electronic configurations, and spin- and optical properties.[28-33] For example, the dithienothiophene-bridged octaphyrin[25] (**2**) exhibits two distinct 26π- and 34π-electron

View Article Online
DOI: 10.1039/D6SC00941G

circuits, which together give rise to bicycloaromatic character. This framework also allows cooperative [4n+1]/[4n+1] electronic mixing upon two-electron oxidation, stabilizing a triplet biradical species with Baird aromaticity. Similarly, fully π-conjugated multicyclic oligothiophenes such as **4** have been reported that feature constituent macrocycles with individual (anti)aromatic character. In this case, electronic coupling in the absence of a dominant π-circuit leads to a change in the overall (anti)aromatic properties upon two-electron oxidation.[34-38] Also known are fully π-conjugated multicyclic molecular cages (**3**) that display oxidation-state-dependent global aromaticity and spin behavior.[39]

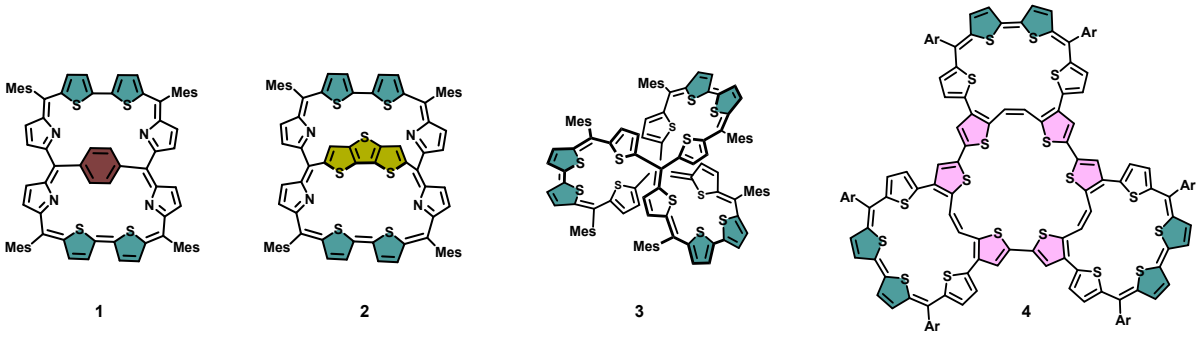

Chart 1. Structure of *para*-phenylene-bridged [34]octaphyrin **1**, dithienothiophene-bridged [34]octaphyrin **2,** 3D aromatic 12-thiophene-cage (c-T12) **3**, and π-conjugated multicyclic macrocycle (3TMC) **4**.

Taken in concert, these contributions serve to highlight the intricate interplay between structural topology, formal oxidation level, and delocalized electronic effects in determining the properties of complex multicyclic conjugated systems. However, approaches that directly enable changes in aromaticity and spin state through intrinsic macrocyclic design remain scarce in fully π-conjugated multicyclic systems. The present study was undertaken in an effort to address this knowledge gap. The availability of N-fused architectures introduced structural asymmetry that offers a rare opportunity to enforce π-electronic reorganization and stabilize open-shell configurations within a single conjugated framework. Against this backdrop, we

View Article Online
DOI: 10.1039/D6SC00941G

developed a straightforward synthetic strategy allowing access to a series of fully π-conjugated asymmetric multicyclic bridged N-fused 36π octaphyrins **5** and **6** incorporating bithiophene and benzithiophene moieties (Scheme 1), which display oxidation- and protonation-responsive electronic and spin-state transformations and corresponding changes in (anti)aromaticity.

Neutral 36π octaphyrins are typically nonaromatic owing to conformational distortion. However, protonation can elicit further changes in electronic structure depending on the nature of the embedded heteroaryl units. In the bithiophene-containing octaphyrin **5**, electronic coupling between the constituent sub-macrocycles stabilizes the triplet state via Baird aromaticity, leading to the formation of a triplet diradical species. In contrast, the benzithiophene-containing analogue **6** displays only a subtle response to protonation, likely due to localized Clar sextet-type stabilization within the phenylene unit in combination with persistent structural distortion, which together favours π-electron localization all over the macrocycle. Also, upon two-electron oxidation, octaphyrins typically exhibit global huckel aromaticity arising from delocalization over a 34π-electron outer circuit. We thus expected that asymmetric octaphyrin-derived multicyclic systems would allow the competing interactions among constituent π-electron circuits to be assessed in detail as a function of external stimulus.

Results and Discussion:

Synthesis and characterization of neutral octaphyrins

The synthesis of core modified *meso*-mesitylene substituted bridged N-fused bithia-bridged 36π bithia-octaphyrin (**5**) and *syn*- and *anti*-benzithia-octaphyrins (**6** and **6'**) is summarized in Scheme 1.[25] Briefly, the required precursors, bithiophene and benzithiophene based tripyrrane (**7** and **8**) and 2,2'-bithiophene-5,5'-dicarboxaldehyde (**9**), were prepared by reported procedures.[40-42] These building blocks were condensed in presence of a catalytic

View Article Online
DOI: 10.1039/D6SC00941G

amount of PTSA, followed by oxidation with 2,3-dichloro-5,6-dicyano-1,4-benzoquinone (DDQ).

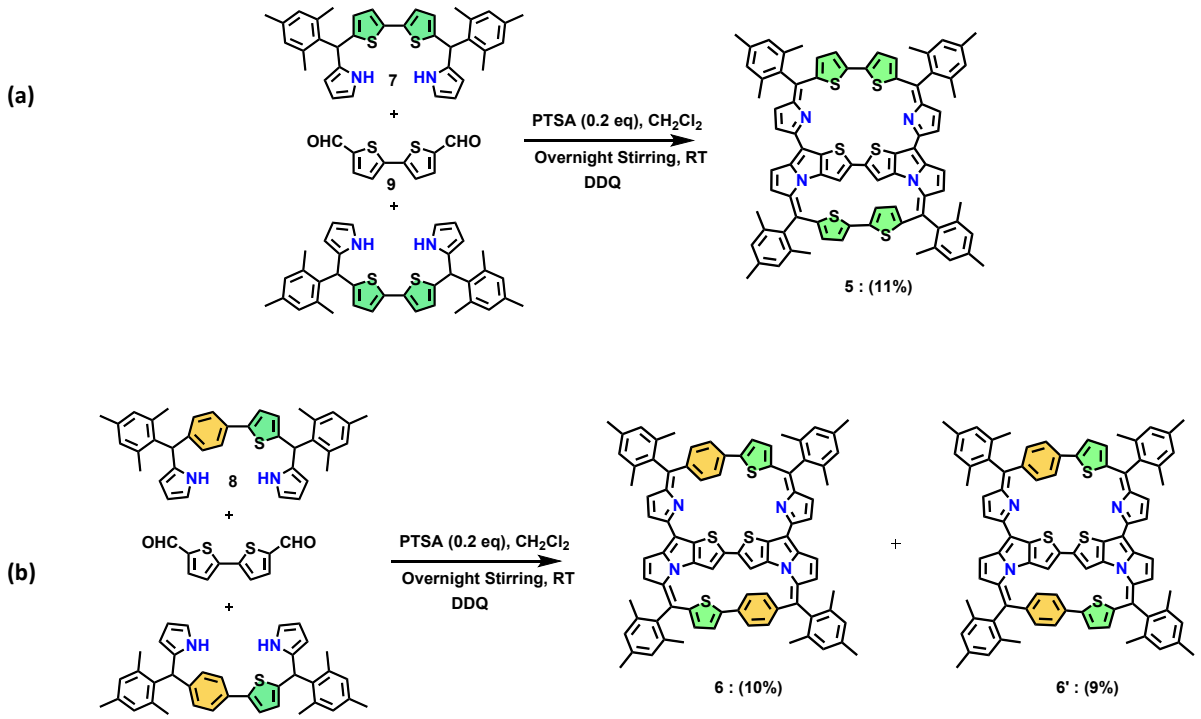

Scheme 1. Synthesis of core modified N-fused bithiophene bridged (a) bithia-octaphyrin (**5**) and (b) benzithia-octaphyrins (**6** and **6'**).

Subsequent column chromatography on basic alumina using CH_2Cl_2/hexanes (40:60) as the eluent afforded the desired brown-colored octaphyrins (**5**, **6**, and **6'**) in 9-11% yield. All three octaphyrins proved soluble in common organic solvents, and their formation was confirmed by standard analytical techniques, including mass spectrometry (MALDI and high-resolution), 1D and 2D NMR, UV-vis, and EPR spectroscopies, as well as through electrochemical and DFT/TD-DFT studies. Octaphyrin **5** was further characterized by means of a single crystal X-ray diffraction analysis.

The ^{1}H NMR spectra of **5**, **6**, and **6′** were recorded in CD_2Cl_2 and $CDCl_3$ respectively (Fig. 1). The signals for **5**, **6**, and **6′** were easily assigned based on their location, integration, coupling

View Article Online
DOI: 10.1039/D6SC00941G

constants, and cross-peak connectivities in the corresponding COSY and ROESY spectra (Figs. S9-S13). Octaphyrin **5** displays a relatively simple spectrum consistent with time-averaged symmetry, with eight *β*-pyrrolic protons appearing as four doublets at 5.89 (h), 6.59 (e), 6.77 (g), and 7.19 ppm (f), and eight *β*-thiophenic protons as four doublets at 6.50 (b), 6.82 (a), 7.10 (d), and 7.36 ppm (c) (Fig. 1a). The fused bithiophene *β*-protons (i) appear as a singlet at 5.40 ppm. In contrast, **6′** retains comparable symmetry but shows electronic perturbation upon benzene incorporation, with the benzene protons (n/n′, r/r′) shifted downfield (7.70 and 7.93 ppm) (Fig. 1c). The four *β*-thiophene protons of **6′** appear as two doublets at 6.72 (k) and 6.42 ppm (l), and the fused-ring *β*-protons (o) resonate significantly downfield at 7.29 ppm. The *anti*-isomer **6** exhibits lower symmetry, giving rise to additional signals; the *β*-pyrrolic protons appear as eight doublets (g, g′, h, h′, i, i′, j, j′), while the *β*-thiophene protons appear as four doublets at 6.67 (l), 7.15 (k), 7.21 (l′), and 7.45 ppm (k′) (Fig. 1b).

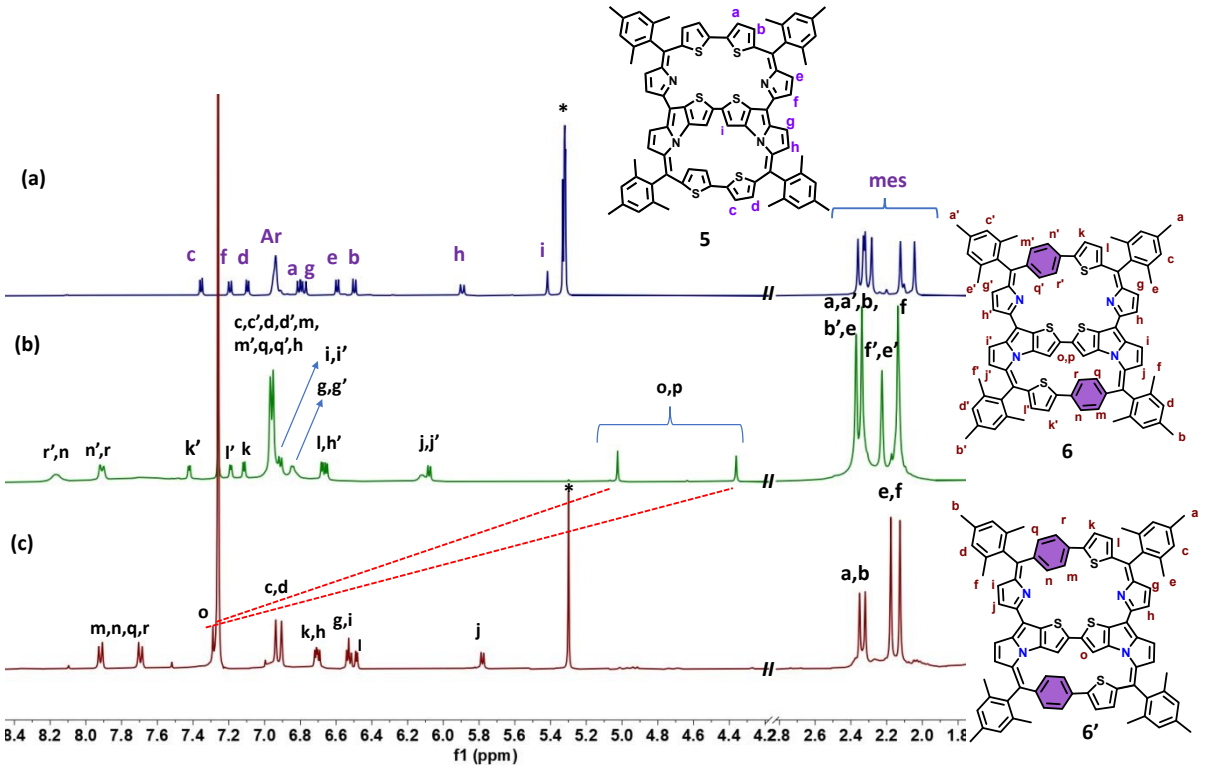

Fig. 1 Comparison of the Partial ^{1}H NMR spectra of macrocycles (a) **5**, recorded in CD_2Cl_2 at -20° C and (b) **6** and (c) **6'** recorded in $CDCl_3$ at 25° C.

View Article Online
DOI: 10.1039/D6SC00941G

Notably, the fused bithiophene β-protons (o,p) in **6** are strongly upfield shifted and split into two singlets at 5.05 and 4.39 ppm.

The fused-ring β-protons located within the macrocyclic cavity serve as sensitive probes of the magnetic environment. In **5**, a moderate upfield shift (5.40 ppm) indicates weak shielding, consistent with the absence of a significant global ring current. In *syn*-configured **6′**, where the two phenylene units are oriented on the same side of the macrocycle, their anisotropic deshielding effects reinforce cooperatively within the cavity, leading to a pronounced downfield shift (7.29 ppm). In contrast, *anti*-configured **6**, containing oppositely oriented phenylene units, exhibits upfield-shifted signals (5.05 and 4.39 ppm), reflecting partial cancellation of the anisotropic contributions and resulting in net shielding at the cavity protons. The pronounced twisting of the benzithiophene units in the lower segment of **6** and **6′** disrupts the macrocyclic conjugation. This suppresses any global ring current and prevents clear differentiation between inner and outer protons in the lower segment. Instead, the observed chemical shifts are dominated by local anisotropic effects. Collectively, the lack of consistent shielding patterns across all three systems supports the absence of global aromaticity. This is in agreement with the computed magnetic criteria (vide infra).

To further validate these observations, ^{1}H NMR chemical shifts were calculated using CAM-B3LYP methods. All core aromatic protons are predicted in the **6–8** ppm region, while the fused bithiophene protons appear at 4.7 ppm for **5** and 3.7–4.6 ppm for **6**, more closely reproducing the experimental shielding trends (Figs. S31-S33). These results further support the dominance of local anisotropic effects over any global ring current.

Diffraction quality single crystals of **5** were grown by slow evaporation of a CH_2Cl_2 solution in a methanol atmosphere at room temperature over seven days (Fig. 2). Under these conditions, octaphyrin analogue **5** crystallizes as a monoclinic system in the I2/a space group. Key crystallographic parameters are provided in Table S1. The crystal structure reveals the

View Article Online
DOI: 10.1039/D6SC00941G

presence of a multicyclic framework containing an N-fused bithiophene bridge, in which the bottom bithiophene unit (E and F units) adopts an up-and-down twisted conformation (Fig. S24). Due to the asymmetric fusion of the bridged-thiophene units, compound **5** adopts two geometrically distinct upper and lower macrocyclic segments (Fig. 2b). The upper constituent macrocycle containing the A~D thiophene units is nearly planar, with the pyrrole and thiophene subunits deviating by only 7.62~14.9° from the mean plane consisting of the six *meso* carbons (C9-C14-C19-C28-C33-C38). On the other hand, the bottom sub-macrocycle is distorted, presumably as the result of the smaller cavity size of the lower macrocycle and the increased steric congestion caused by the asymmetrically fused bridge (Fig. 2b).

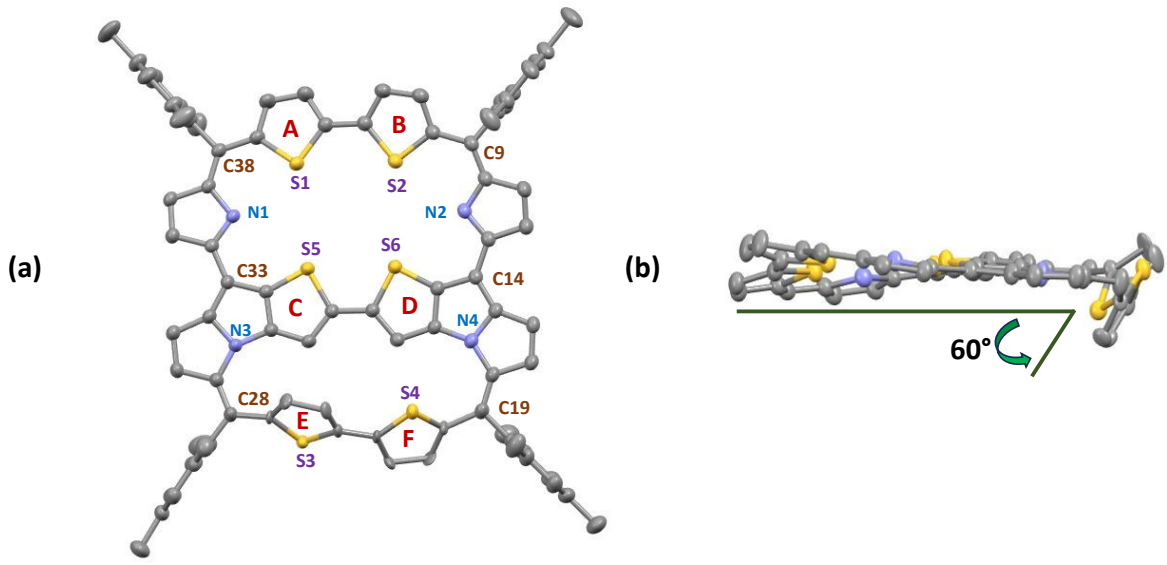

Fig. 2 X-ray crystal structure of **5:** (a) Top view, (b) side view. The thermal ellipsoids are scaled to the 40% probability level. *Meso*-aryl groups and hydrogen atoms are omitted for clarity. (CCDC No. of **5** 2432301).

This distortion is manifest in the large dihedral angles of 62.4° and 53.6°, respectively, between the E and F thiophene units. The *meso*-mesitylene groups are also oriented almost perpendicular to the octaphyrin plane with dihedral angles of 76.8~84.9°. These latter

View Article Online
DOI: 10.1039/D6SC00941G

substituents were thus expected to have a negligible effect on the π-conjugation of the polycyclic core.

Octaphyrins **6** and **6'** are insufficiently stable to afford diffraction-quality single crystals; thus, the structural and electronic features of **5**, **6**, and **6'** were evaluated using DFT calculations in conjunction with magnetic and spectroscopic analyses (Fig. S26). The optimized structure of **5** reveals pronounced distortion, with the bottom bithiophene unit (thiophenes E and F) oriented nearly perpendicular (~90°) to the mean macrocyclic plane (Fig. S26a). Although the molecule retains overall C_2 symmetry, this orthogonal arrangement severely limits π-overlap along the macrocyclic pathway, effectively disrupting conjugation. A similar but more pronounced effect is observed in **6** and **6'**, where incorporation of bulky phenylene units enforces an obliquely distorted elliptical geometry and introduces additional torsional strain (Fig. S26(b,c)). As a result, continuous π-delocalization around the macrocycle is structurally inhibited in all three systems.

This disruption of conjugation is directly reflected in their magnetic properties. The $NICS_{zz}(2)$[43] values within the macrocyclic cores of **5**, **6**, and **6'** are close to zero, indicating negligible global ring current effects (Figs. 3b–d). Consistently, ACID[44] analyses show no continuous diatropic current along the macrocyclic perimeter, confirming the absence of global aromaticity (Fig. S34). These findings are in agreement with the ^{1}H NMR spectra, which show no significant upfield or downfield shifts attributable to a global ring current, further supporting a nonaromatic macrocyclic framework. Instead, current density is localized within individual subunits, particularly the phenylene rings in **6** and **6'**, highlighting that aromaticity is confined to local fragments rather than the macrocycle as a whole.

These electronic consequences of structural distortion are further manifested in the optical properties. The UV–vis–NIR spectra of **5**, **6**, and **6'** exhibit similar absorption features, with an intense band at 465–480 nm and only weak, diffuse absorption extending into the NIR

View Article Online
DOI: 10.1039/D6SC00941G

region (Fig. 3a). Such spectral profiles lack the intense, low-energy transitions characteristic of globally aromatic expanded porphyrins and are instead consistent with systems in which conjugation is interrupted[13,30]. TD-DFT calculations reproduce these features (Fig. S55), reinforcing the conclusion that torsional distortion and loss of effective π-overlap suppress global aromaticity in **5**, **6**, and **6'**. Compound **6′**, owing to its lower stability, was limited to neutral-state characterization but serves as a structural analogue supporting the intrinsic localization behavior of the benzithiophene framework**.**

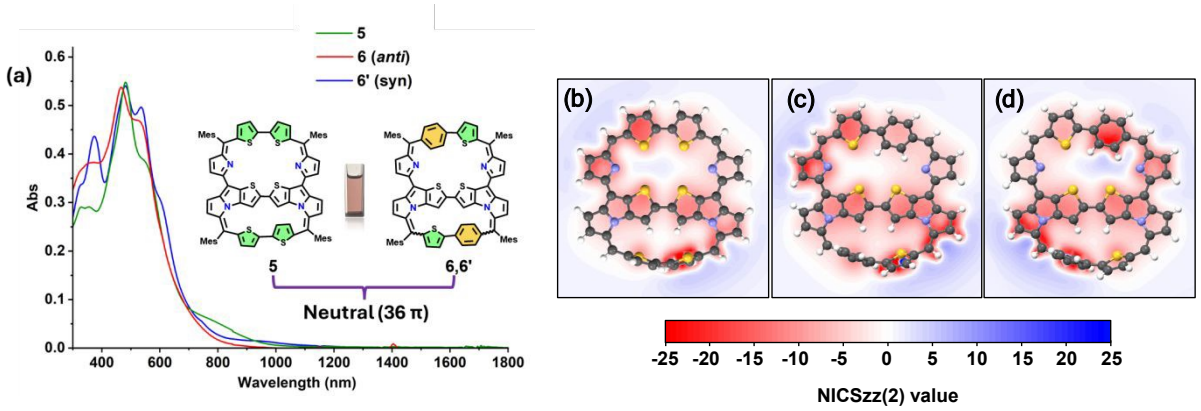

Fig. 3 (a) Comparison of absorption spectra and NICSzz(2) scans of the neutral forms of octaphyrins (b) **5**, (c) **6** (*anti*) and (d) **6'** (*syn*).

Protonation-Driven Access to Baird Aromaticity

To elucidate how environmental perturbations modulate the π-electronic structure and aromaticity of multicyclic octaphyrins, compounds **5** and **6** were treated with trifluoroacetic acid (TFA). Protonation elicited strikingly disparate UV–vis–NIR spectral responses for the two systems (Fig. 4). For **5**, protonation induced the emergence of an additional intense absorption band at 623 nm and a broad NIR feature centered at 1085 nm and extending beyond 1400 nm (Fig. 4a). This spectral signature closely resembles that of the corresponding two-electron-oxidized species $[\mathbf{5}]^{2+}$, which is discussed below, exhibits the characteristic B- and Q-like band structure of aromatic porphyrinoids.[15-16] In contrast, protonation of **6** resulted only in

View Article Online
DOI: 10.1039/D6SC00941G

a modest red shift, with the overall spectral profile remaining nearly identical to that of its neutral, nonaromatic form. These distinct responses were further supported by femtosecond transient absorption (fs-TA) measurements (Figs. S25(a-b, e–f)). Upon protonation, **5** exhibited a substantial increase in the excited-state lifetime from 5.5 to 14 ps, whereas **6** showed only a comparatively minor change from 10.5 to 12.3 ps. Collectively, these observations lead us to conclude that protonation induces profound π-electronic reorganization and aromatic enhancement in **5**, whereas **6** experiences only minor perturbations.

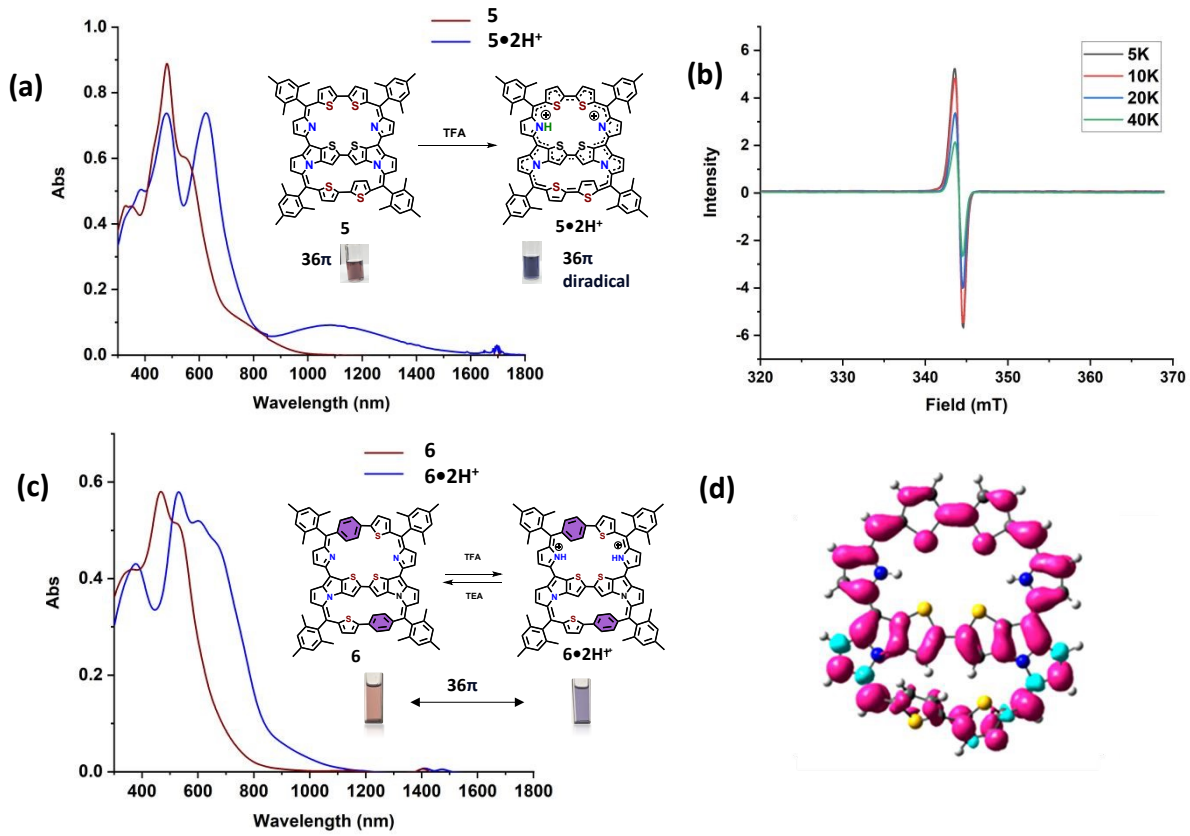

Fig. 4 UV–vis–NIR absorption spectra of (a) **5** and (c) **6** in CH_2Cl_2 observed upon protonation with CF_3COOH. (b) EPR spectrum of the protonated form of **5** (**5•2H**$^+$) recorded in toluene at different temperatures from 5 K to 40K. (d) Mulliken electron spin density plot of **5•2H**$^+$ in the T_1 state.

View Article Online
DOI: 10.1039/D6SC00941G

The ^{1}H NMR spectra of the protonated species **5•2H$^+$**, and **6•2H$^+$**, were recorded in $CDCl_3$. spectra of **5•2H$^+$** were acquired at variable temperatures, whereas **6•2H$^+$**, were recorded at room temperature with varying concentrations of TFA (Figs. S14 and S15). For **5•2H$^+$**, no discernible resonances other than broad mesityl signals at 2.0–2.5 ppm were observed (Fig. S14). This finding is consistent with the presence of unpaired electrons and an accessible triplet ground state.[45-46] Upon neutralization with triethylamine (TEA), the original ^{1}H NMR spectrum of neutral **5** was fully restored. Considering the reversible acid–base behavior and the redox potentials, the featureless NMR spectrum of **5•2H$^+$** provides compelling evidence that protonation alone generates a radical species.[45] In contrast, the ^{1}H NMR spectrum of **6•2H$^+$** exhibited β-proton resonances from the pyrrole and thiophene subunits between 6.2 and 7.7 ppm (Fig. S15), with only small chemical shift perturbations relative to the neutral form. The absence of the characteristic shielding/deshielding pattern associated with global ring currents leads us to suggest that protonation of **6** does not alter its overall electronic structure.

To substantiate the open-shell nature of **5•2H$^+$**, variable-temperature EPR measurements (5–40 K) were conducted (Fig. 4b). A broad isotropic signal with a g value of 1.973 was observed, consistent with a highly delocalized and symmetric spin distribution. The signal intensity increased upon cooling, in accordance with Curie's law, indicating a triplet ground state. Fitting the data to the Bleaney–Bowers equation yielded a singlet–triplet energy gap ($\Delta E_{S\text{-}T}$) of 0.013 kcal mol^{-1}, leading us to propose that the triplet state is thermally accessible at ambient temperature in the presence of TFA (Fig. S16).

To gain mechanistic insight into the divergent electronic responses upon protonation, DFT calculations were performed on **5•2H$^+$** and **6•2H$^+$**. For **5•2H$^+$**, optimization in the T_1 state reveals a substantial reduction in the dihedral angle of the bithiophene segment and pronounced planarization of the macrocycle (Fig. 5a and S28a), restoring effective π-overlap

View Article Online
DOI: 10.1039/D6SC00941G

and enabling a continuous conjugation pathway absent in the neutral state. The Mulliken spin density confirms extensive delocalization of unpaired electron density across the framework, while comparatively lower spin density is observed over the lower bithiophene unit due to its distorted geometry (Fig. 4d and S16c), consistent with the open-shell character of the system. In contrast, **6•2H$^+$** retains significant torsional distortion in the S_0 state, with a geometry similar to its neutral form (Fig. 5b, S28b), preventing effective π-overlap and limiting conjugation to localized segments. As a result, **6•2H$^+$** remains closed-shell. These differences are reflected in the calculated singlet–triplet gaps: **5•2H$^+$** exhibits a relatively small ΔE_{S-T} (6.2 kcal mol^{-1}) (Table S12-S13), consistent with accessible triplet character, whereas **6•2H$^+$** shows a much larger gap (16.5 kcal mol^{-1}) (Table S10-11), indicating stabilization of the closed-shell ground state due to inhibited π-delocalization.

Further insight is provided by NICS and ACID analyses. For **5•2H$^+$** in the T_1 state, the $NICS_{zz}(2)$ map shows predominantly negative values (~ –25) (Fig. 5c and S39c) across the macrocyclic core, and ACID plot (Fig. S36a and S37c) reveal a continuous diatropic current pathway, primarily along the upper macrocyclic segment with an additional contribution from the outer circuit. These features are characteristic of a conjugation-enabled ring current in the triplet state and are consistent with Baird aromaticity, enabled by protonation-induced planarization that restores effective π-overlap. In contrast, **6•2H$^+$** displays NICS value (Fig. 5d and S40c) close to zero across the macrocycle, with ACID plot (Fig. S36b and S38c) showing current density localized within the phenylene subunits rather than along the macrocyclic perimeter.

View Article Online
DOI: 10.1039/D6SC00941G

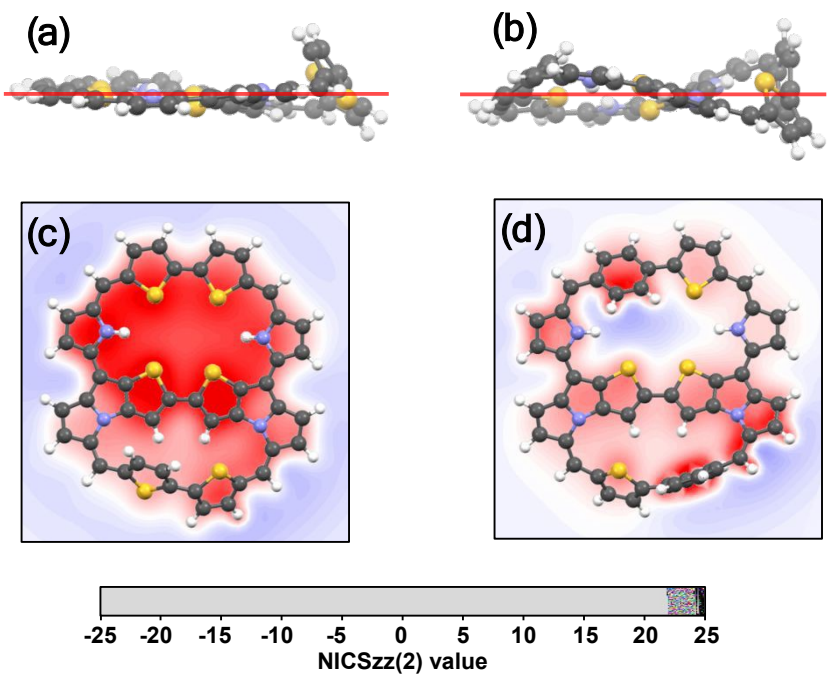

Fig. 5 Optimized structures of (a) **5•2H**$^+$ in the T_1 state and (b) **6•2H**$^+$ in the S_0 state shown in side views. In the side view, the red lines indicate the molecular mean plane. NICSzz(2) map for (c) **5•2H**$^+$ in the T_1 state and (d) **6•2H**$^+$ in the S_0 state.

Furthermore, upon protonation, the calculated HOMA (Harmonic Oscillator Model of Aromaticity)[47] values increase from 0.64 for neutral **5** to ~0.81–0.82 for **5•2H$^+$**, whereas the benzithia analogue **6** shows essentially no appreciable change (0.63 for both neutral and protonated forms) (Figs. S43-S44). Consistently, the bond-length alternation (BLA) values decrease significantly from 0.065 Å for neutral **5** to 0.026–0.042 Å for **5•2H$^+$**, while only a modest reduction is observed for the benzithia system (0.064 to 0.056 Å for **6** and **6•2H$^+$**, respectively), indicating substantially greater bond equalization and π-delocalization in the bithia framework. While HOMA is parameterized for monocyclic systems and may not fully capture aromaticity in extended multicyclic frameworks, the observed increase in **5•2H$^+$** is primarily associated with a marked reduction in the GEO (bond-length alternation) term, whereas the EN (average bond-length deviation) term changes only minimally. These trends are fully consistent with the magnetic aromaticity analyses and indicate that protonation-

View Article Online
DOI: 10.1039/D6SC00941G

induced planarization, together with stabilization of an open-shell electronic structure, restores effective π-overlap and promotes the emergence of Baird-type aromaticity in **5•2H$^+$**. In contrast, the benzithia system **6•2H$^+$** retains dominant Clar sextet-type local aromatic stabilization, which enforces π-electron localization and suppresses the development of a continuous macrocyclic conjugation pathway. As a consequence, global delocalization is inhibited and the triplet state is not effectively stabilized, consistent with the comparatively large singlet–triplet energy gap.

Oxidation-Controlled Global Hückel Aromaticity

A distinctive feature of octaphyrins **5**, **6**, and **6'** lies in their asymmetric multicyclic frameworks, which accommodate three formal π-conjugation pathways involving the upper, lower, and outermost macrocyclic circuits. The interplay among these conjugation modes is expected to dictate the overall π-electronic structure of these systems. To elucidate this interplay, compounds **5** and **6** were subjected to controlled oxidation, whereas similar studies on **6'** were precluded by its limited stability.

Cyclic voltammetry (CV) revealed that both **5** and **6** exhibit comparable redox behavior (Figs. 6a-6b and S18–S19). The CV reveals four oxidation events and one reduction process at 0.11, 0.28, 1.00, 1.28, and –1.20 V (vs. Ag/Ag$^+$) for **5**, and at 0.22, 0.38, 1.09, 1.30, and –1.34 V (vs. Ag/Ag$^+$) for **6**. Considering the oxidation potential of $NOSbF_6$ (0.35 V vs Ag/Ag$^+$), this reagent was selected to achieve two-electron oxidation of both systems. Oxidation with $NOSbF_6$ induced pronounced changes in the UV–vis–NIR absorption spectra of **5** and **6** (Fig. 6c and 6d). Moreover, spectroelectrochemical measurements at the second oxidation potentials (0.45 V for **5** and 0.51 V for **6**) produced spectral changes analogous to those obtained under chemical oxidation (Figs. S18–S19), thus supporting the inference that $NOSbF_6$ treatment indeed affords the corresponding two-electron oxidized species.

View Article Online
DOI: 10.1039/D6SC00941G

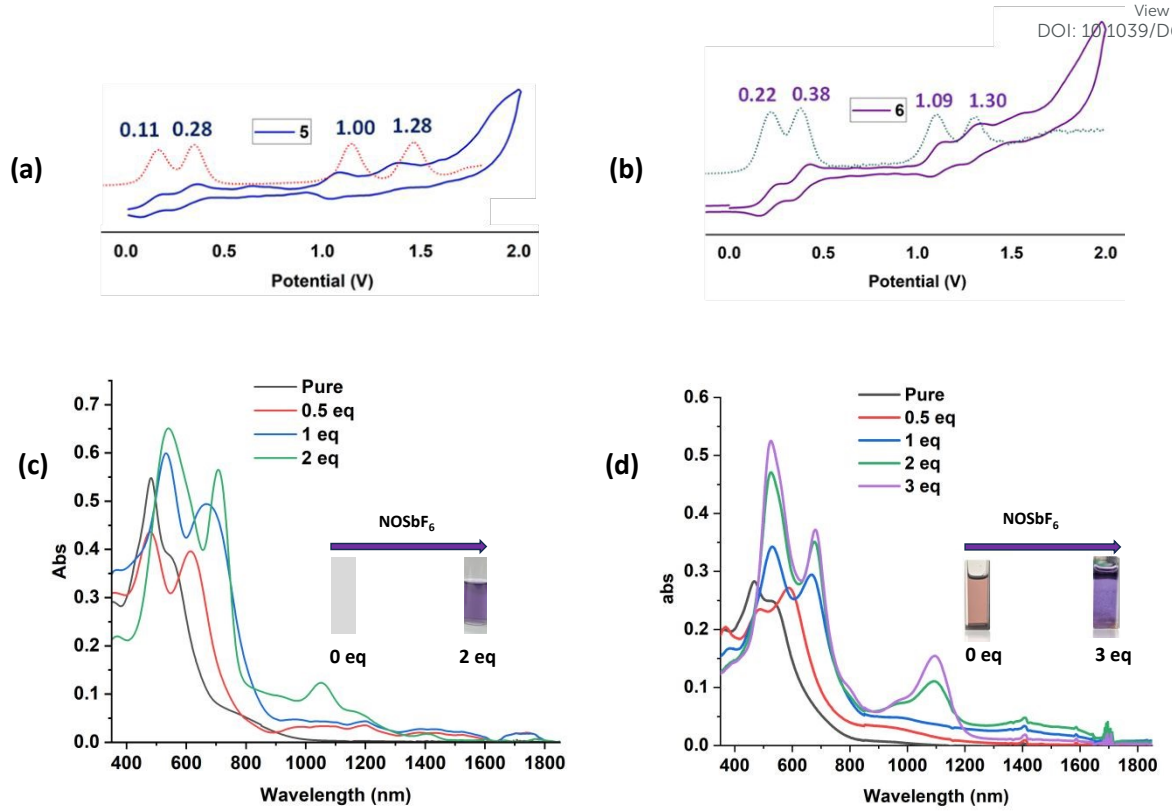

Fig. 6 Cyclic voltammograms and differential pulse voltammograms corresponding to the oxidation of macrocycles (a) **5** and (b) **6** recorded in CH_2Cl_2 using $TBAPF_6$ (0.1 M) as the supporting electrolyte, $Ag/AgNO_3$ as the reference electrode, and a scan rate of 100 mV/s at 25 °C. UV–vis–NIR absorption spectra of the two-electron oxidized form of macrocycle (c) **5** (10^{-5} M) and (d) **6** (10^{-5} M) obtained by chemical oxidation with $NOSbF_6$ in CH_2Cl_2.

The dications $\mathbf{[5]^{2+}}$ and $\mathbf{[6]^{2+}}$ display absorption bands that extend well into the NIR region, with features observable up to ~1200 nm (Fig. 6). Upon stepwise addition of two equivalents of $NOSbF_6$, both macrocycles undergo a distinct color change from brown to purple, accompanied by pronounced red-shifts in their absorption maxima. In $\mathbf{[5]^{2+}}$ new peaks appear at 536 and 711 nm, whereas $\mathbf{[6]^{2+}}$ exhibits corresponding bands at 525 and 682 nm and a broad Q-like transition centered at 1098 nm (Figs 6c–d). Both dications show enhanced molar absorptivities above 500 nm compared to their neutral counterparts and display spectral signatures characteristic of aromatic porphyrinoids—namely, an intense B-like band

View Article Online
DOI: 10.1039/D6SC00941G

accompanied by weaker Q-like transitions.[15-17] Femtosecond transient absorption (fs-TA) measurements further revealed prolonged excited-state lifetimes for the oxidized species relative to their neutral analogues, with **[5]**$^{2+}$ and **[6]**$^{2+}$ exhibiting decay components of 17 and 15 ps, respectively (Figs. S25(c-d)), indicating enhanced excited-state stabilization upon oxidation.[25,30]

Additional confirmation of the dicationic and aromatic nature of **[5]**$^{2+}$ and **[6]**$^{2+}$ was obtained from high-resolution mass spectrometric (HRMS) and NMR spectroscopic analyses (Figs. S20–S23). The HRMS spectra were characterized by molecular ions consistent with the proposed dicationic structures, while the NMR spectra revealed low-field resonances (9.0–11.0 ppm for **[5]**$^{2+}$ and 9.5–13.0 ppm for **[6]**$^{2+}$) indicative of diatropic ring currents associated with global aromaticity. Signals corresponding to the thiophene (*c* and *d*) for **[5]**$^{2+}$ and core benzene protons for **[6]**$^{2+}$ were not observed, likely due to fluxional behavior of the peripheral rings. The fused thiophene protons in **[5]**$^{2+}$ overlap with mesityl CH resonances at ~7.4 ppm, whereas those in **[6]**$^{2+}$ appear further downfield (7.87 and 8.21 ppm). Both findings are consistent with strong macrocyclic aromatic ring currents.

To determine whether appreciable oxidation-induced structural reorganization occurs, DFT calculations were performed on simplified models of **[5]**$^{2+}$ and **[6]**$^{2+}$. Geometry optimizations revealed substantial planarization upon oxidation, particularly in the lower regions of the macrocycles containing the flexible bithienyl (**5**) and benzithienyl (**6**) units (Figs. 7, and S27). In their neutral states, these fragments are highly twisted relative to the macrocyclic plane, with dihedral angles of 90.0° (**5**) and 88.9° (**6**) (Fig. S26). Upon two-electron oxidation, these angles decrease to 45.4° in **[5]**$^{2+}$ and 54.3° in **[6]**$^{2+}$, while the remaining macrocyclic framework becomes nearly coplanar (Fig. S27). This pronounced

View Article Online
DOI: 10.1039/D6SC00941G

planarization is consistent with enhanced π-electron delocalization being present upon oxidation.

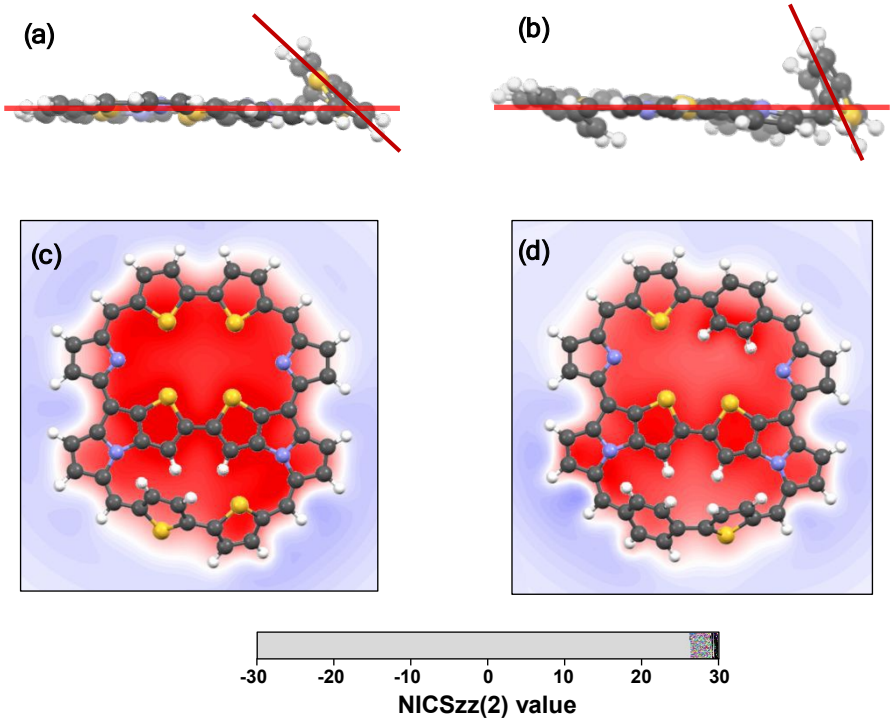

Fig. 7 Side view of optimized structures of (a) $[\mathbf{5}]^{2+}$ and (b) $[\mathbf{6}]^{2+}$. NICSzz(2) scan of (c) $[\mathbf{5}]^{2+}$ and (d) $[\mathbf{6}]^{2+}$.

Theoretical aromaticity indices corroborate the suggestion that enhanced π-electron delocalization is induced upon oxidation. NICSzz(2) scans across the molecular plane revealed strongly negative values (≈ –30 for $[\mathbf{5}]^{2+}$ and ≈ –20 for $[\mathbf{6}]^{2+}$) throughout the macrocyclic core, consistent with pronounced diatropic ring currents along the outermost π-conjugation pathway (Figs. 7c–d). ACID plots visually confirmed these results, showing a dominant clockwise ring current around the macrocyclic periphery (Fig. S35).

Furthermore, the calculated HOMA (Harmonic Oscillator Model of Aromaticity) values increase upon oxidation from 0.64 and 0.63 for neutral **5** and **6**, respectively, to ~0.80–0.82 and ~0.69 for the corresponding dications, indicating enhanced bond-length equalization

View Article Online
DOI: 10.1039/D6SC00941G

(Fig. S43-S44). Consistently, the bond-length alternation (BLA) values decrease from 0.065 and 0.064 Å for neutral **5** and **6**, respectively, to 0.041–0.042 and 0.052 Å for the corresponding oxidized species, reflecting suppression of bond alternation and increased π-delocalization. Taken together, these results demonstrate that two-electron oxidation converts the formally 36π system into a 34π (4n+2) framework and, concomitant with oxidation-induced planarization, restores effective π-overlap to enable a continuous cyclic conjugation pathway, thereby giving rise to globally aromatic [34]π octaphyrin species.

Interplay of Competing π-Electronic Circuits in Aromaticity Switching

In the neutral state, although compounds **5** and **6** formally possess a 36π-electron framework, effective macrocyclic conjugation is not realized due to disruption of π-electronic communication between submacrocycles, leading to a globally nonaromatic ground state. EDDB[48(a,b)] analysis reveals fragmented delocalization, with electron density largely confined to individual subunits (Fig. S45). Although the upper segment of **5** retains a locally aromatic 26π core-modified hexaphyrin (rubyrin-like) motif[49,50] (Fig. S53), the lower segment remains electronically decoupled, as evidenced by HOMO localization (Fig. S54), thereby preventing continuous cyclic conjugation and rendering the formal 36π count ineffective.

Upon protonation, compound **5** undergoes pronounced π-electronic reorganization enabled by its structurally flexible bithiophene unit. Partial planarization and quinoidal distortion facilitate enhanced π-overlap, allowing delocalization of unpaired electron density across the macrocycle and stabilizing an open-shell triplet state (Fig. 8).[32,51,52(a,b)] This tendency toward open-shell character arises from the inherent instability of the 36π-electron (4n) conjugation pathway in the singlet ground state (S_0), consistent with Hückel antiaromaticity (Fig. S41-S42). The resulting electronic destabilization promotes spin-state reorganization, facilitating access to a lower-energy triplet configuration in accordance with Baird aromaticity. This is consistent

View Article Online
DOI: 10.1039/D6SC00941G

with its relatively small HOMO–LUMO gap (ΔE_{H-L} = 1.56 eV, decreasing to 0.48 eV upon protonation), which promotes diradical character. The resulting conjugation pathway supports triplet-state aromaticity, with dominant contributions from the upper rubyrin segment and the outer macrocyclic circuit. In contrast, **6•2H**$^+$ remains electronically localized due to the rigidity of the benzithiophene unit and the persistence of strong Clar sextet stabilization within the phenylene rings.[53] This suppresses quinoidal reorganization and maintains a larger HOMO–LUMO gap (ΔE_{H-L} = 1.56 eV), favoring a closed-shell configuration and preventing the emergence of global delocalization and triplet aromaticity.

Consistent with this behavior, replacement of one thiophene unit by a benzene ring leads to a longer excited-state lifetime in neutral **6** (10.5 ps) compared to **5** (5.5 ps), reflecting increased clar sextet stabilization and reduced nonradiative relaxation associated with the phenylene subunit. Moreover, upon protonation, **5•2H**$^+$ exhibits a substantial increase in excited-state lifetime (14 ps), whereas only a comparatively minor change is observed for **6•2H**$^+$ (12.3 ps), indicating that the excited-state electronic structure of **6** is already relatively stabilized and undergoes only limited π-electronic reorganization.

Upon oxidation, both systems **[5]**$^{2+}$ and **[6]**$^{2+}$ exhibit global aromaticity, driven by the establishment of a 34π (4n+2) electron framework (Fig. 8). This electron count provides a strong thermodynamic driving force for aromatic stabilization, and to maximize this stabilization both systems undergo structural reorganization toward more planar conformations, enhancing π-overlap and enabling continuous delocalization along the outer conjugation pathway. In the case of **5**, oxidation is accompanied by a decrease in the HOMO–LUMO gap (from 1.56 eV in the neutral form to 1.22 eV in the oxidized state), consistent with

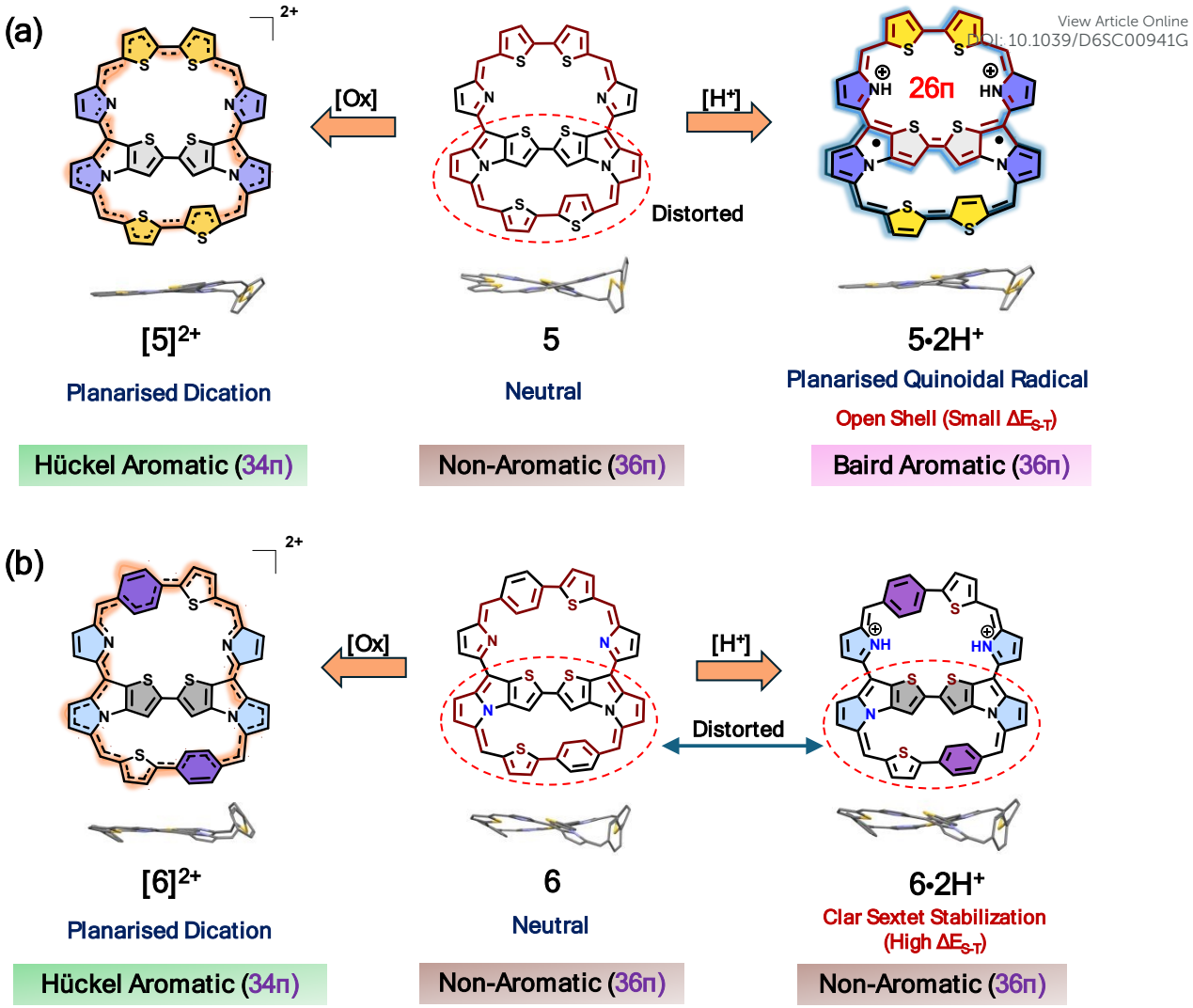

Fig. 8 Schematic illustration of the interplay of π-electronic circuits and molecular aromaticity in asymmetric multicyclic N-fused 36π octaphyrins (a) **5** and (b) **6**.

enhanced π-delocalization (Fig. S49). Similarly, for **6**, the HOMO–LUMO gap decreases from 1.83 eV to 1.16 eV upon oxidation, reflecting increased electronic delocalization associated with the aromatic state (Fig. S50). In the case of $[\mathbf{6}]^{2+}$, although the benzithiophene segments intrinsically favor localized aromatic stabilization, oxidation shifts the balance toward macrocyclic delocalization. The extension of conjugation along the outer π-circuit becomes energetically dominant, allowing the system to sustain a continuous diatropic ring current. Femtosecond transient absorption (fs-TA) measurements further support this electronic reorganization, with $[\mathbf{6}]^{2+}$ exhibiting a prolonged excited-state lifetime of 15 ps (Fig. S25),

View Article Online
DOI: 10.1039/D6SC00941G

indicative of enhanced excited-state stabilization upon oxidation Accordingly, global aromaticity in **[6]**$^{2+}$ arises from the overriding influence of the macrocyclic π-framework over competing localized interactions.

Conclusion

In summary, this work presents a new class of fully π-conjugated asymmetric multicyclic N-fused 36π octaphyrins that serve as a well-defined platform for elucidating complex aromatic phenomena. Structural asymmetry and electronically differentiated subunits were shown to enable precise, stimulus-responsive modulation of aromaticity and spin states. In their neutral forms, these macrocycles are globally nonaromatic; however, protonation induces markedly divergent electronic responses. In the bithiophene-embedded octaphyrin, strong interunit π-coupling promotes triplet-state stabilization through Baird-typed aromaticity, whereas in the benzithiophene analogue, the combination of persistent Clar sextet stabilization within the phenylene unit and significant structural distortion favors π-electron localization over macrocyclic delocalization, resulting in minimal structural and electronic changes. Upon two-electron oxidation, both systems undergo a distinct transformation into strongly aromatic 34π-electron frameworks. Collectively, these results establish a general design principle in which aromaticity can be tuned through the interplay of competing local and global π-electronic circuits governed by structural flexibility and electron count. The ability to reversibly access nonaromatic, Hückel-aromatic, and Baird-aromatic states within a single molecular framework provides a foundation for designing π-conjugated systems with controllable electronic structure. Such tunable aromaticity offers opportunities for the development of responsive molecular switches, NIR-active materials, and spin-dependent electronic systems, where precise control over delocalization and spin topology is essential.

View Article Online
DOI: 10.1039/D6SC00941G

Data Availability

The data supporting this article has been included as part of the ESI. CCDC No. of **5** 2432301.

AUTHOR INFORMATION

Corresponding Authors

*Juwon Oh- Department of Chemistry and Green-Nano Material Research Center, Kyungpook National University, Daegu 41566, Korea; Department of Chemistry, Soonchunhyang University, Asan 31538, Korea: Email: juwoh933@knu.ac.kr

*Woo-Dong Jang- Department of Chemistry, Yonsei University, 50 Yonsei-ro, Seodaemun-gu, Seoul 03722, Republic of Korea; orcid.org/0000-0002-1281-6037; Email: wdjang@yonsei.ac.kr

*Dongho Kim- Department of Chemistry, Yonsei University, 50 Yonsei-ro, Seodaemun-gu, Seoul 03722 Email: dongho@yonsei.ac.kr

Authors

Dr. Md Ashif Ali- Department of Chemistry, Yonsei University, 50 Yonsei-ro, Seodaemun-gu, Seoul 03722, Republic of Korea.

Ji Heon Kim- Department of Chemistry and Green-Nano Material Research Center, Kyungpook National University, Daegu 41566, Korea

Dr. Younghun Kim- Department of Chemistry, Yonsei University, 50 Yonsei-ro, Seodaemun-gu, Seoul 03722, Republic of Korea.

Yunwoo Nam- Department of Chemistry, Yonsei University, 50 Yonsei-ro, Seodaemun-gu, Seoul 03722, Republic of Korea.

Author contributions

M.A.A.: Conceptualization, Synthesis, Methodology, Investigation, Formal analysis, Data curation, Writing – original draft. J.H.K.: Formal analysis, Methodology, Validation (DFT calculations). Y.K.: Investigation, Formal analysis (single-crystal X-ray diffraction). Y.N.:

View Article Online
DOI: 10.1039/D6SC00941G

Investigation, Formal analysis (electrochemical measurements). J.O.: Supervision, Writing – review & editing. W.-D.J.: Supervision, Funding acquisition, Resources, Writing – review & editing. D.K.: Conceptualization, Supervision, Funding acquisition, Project administration, Resources, Writing – review & editing.

Conflicts of interest

The authors declare no competing financial interest.

Acknowledgment

M.A.A thanks Yonsei University Research Fund (Yonsei University Frontier Fellowship 2023 and BK21 2024-25 Fellowship). J.O. thanks the NRF funded by the Korea Government (MSIT) (RS-2024-00343229, 2021R1A6A1A03039503 and RS-2024-00404760). W.-D.J thanks National Research Foundation (NRF) grants (RS-2025-00514482) funded by the Ministry of Science and ICT (MSIT), Korea. D.K thanks the National Research Foundation of Korea (NRF) grant funded by the Korea government (MSIT) (No. RS-2020-NR049542).

Notes and references

1. E. Hückel and Q. B. zum Benzolproblem, *Z. Phys.*, 1931, **70**, 204–286.
2. M. K. Cyrański, *Chem. Rev.*, 2005, **105**, 3773–3811.
3. O. El Bakouri, J. Poater, F. Feixas and M. Solà, *Theor. Chem. Acc.*, 2016, **135**, 205.
4. M. Solà, *Front. Chem.*, 2013, **1**, 22.
5. G. Portella, J. Poater and M. Sola, *J. Phys. Org. Chem.*, 2005, **18**, 785–791.
6. (a) T. D. Lash, *Chem. Rev.*, 2017, **117**, 2313–2446. (b) S. Saito and A. Osuka, *Angew. Chemie Int. Ed.*, 2011, **50**, 4342–4373.
7. M. Jirásek, H. L. Anderson and M. D. Peeks, *Acc. Chem. Res.*, 2021, **54**, 3241–3251.
8. Y. Nakagami, R. Sekine and J. Aihara, *Org. Biomol. Chem.*, 2012, **10**, 5219–5229.

9. J. L. Sessler, D.-G. Cho, M. Stępień, V. Lynch, J. Waluk, Z. S. Yoon and D. Kim, *J. Am. Chem. Soc.*, 2006, **128**, 12640–12641.

10. T. Tanaka and A. Osuka, *Chem. Rev.*, 2017, **117**, 2584–2640.

11. V. G. Anand, S. K. Pushpan, S. Venkatraman, A. Dey, T. K. Chandrashekar, B. S. Joshi, R. Roy, W. Teng and K. R. Senge, *J. Am. Chem. Soc.*, 2001, **123**, 8620–8621.

12. M. D. Peeks, T. D. W. Claridge and H. L. Anderson, *Nature*, 2017, **541**, 200–203.

13. H. Rath, J. Sankar, V. PrabhuRaja, T. K. Chandrashekar, B. S. Joshi and R. Roy, *Chem. Commun.*, 2005, 3343–3345.

14. Y. Rao, L. Xu, M. Zhou, B. Yin, A. Osuka and J. Song, *Angew. Chemie Int. Ed.*, 2022, **61**, e202206899.

15. J.-Y. Shin, K. S. Kim, M.-C. Yoon, J. M. Lim, Z. S. Yoon, A. Osuka and D. Kim, *Chem. Soc. Rev.*, 2010, **39**, 2751–2767.

16. J. Mack, *Chem. Rev.*, 2017, **117**, 3444–3478.

17. C. Liu, M. E. Sandoval-Salinas, Y. Hong, T. Y. Gopalakrishna, H. Phan, N. Aratani, T. S. Herng, J. Ding, H. Yamada, D. Kim, D. Casanova and J. Wu, *Chem*, 2018, **4**, 1586–1595.

18. M. Ishida, S.-J. Kim, C. Preihs, K. Ohkubo, J. M. Lim, B. S. Lee, J. S. Park, V. M. Lynch, V. V Roznyatovskiy, T. Sarma, P. K. Panda, C.-H. Lee, S. Fukuzumi, D. Kim and J. L. Sessler, *Nat. Chem.*, 2013, **5**, 15–20.

19. N. C. Baird, *J. Am. Chem. Soc.*, 1972, **94**, 4941–4948.

20. C. Liu, Y. Ni, X. Lu, G. Li and J. Wu, *Acc. Chem. Res.*, 2019, **52**, 2309–2321.

21. M. Solà, *WIREs Comput. Mol. Sci.*, 2019, **9**, e1404.

22. M. Rosenberg, C. Dahlstrand, K. Kilsa and H. Ottosson, *Chem. Rev.*, 2014, **114**, 5379–5425.

23. J. Kim, J. Oh, A. Osuka and D. Kim, *Chem. Soc. Rev.*, 2022, **51**, 268–292.

View Article Online
DOI: 10.1039/D6SC00941G

24. G. Karthik, W.-Y. Cha, A. Ghosh, T. Kim, A. Srinivasan, D. Kim and T. K. Chandrashekar, *Chem. – An Asian J.*, 2016, **11**, 1447–1453.

25. W.-Y. Cha, T. Kim, A. Ghosh, Z. Zhang, X.-S. Ke, R. Ali, V. M. Lynch, J. Jung, W. Kim, S. Lee, S. Fukuzumi, J. S. Park, J. L. Sessler, T. K. Chandrashekar and D. Kim, *Nat. Chem.*, 2017, **9**, 1243–1248.

26. Y. Ni, T. Y. Gopalakrishna, H. Phan, T. Kim, T. S. Herng, Y. Han, T. Tao, J. Ding, D. Kim and J. Wu, *Nat. Chem.*, 2020, **12**, 242–248.

27. L. Ren, Y. Han, X. Hou, Y. Ni, Y. Zou, T. Jiao and J. Wu, *J. Am. Chem. Soc.*, 2023, **145**, 12398–12406.

28. V. G. Anand, S. Saito, S. Shimizu and A. Osuka, *Angew. Chemie Int. Ed.*, 2005, **44**, 7244–7248.

29. T. Woller, J. Contreras-García, P. Geerlings, F. De Proft and M. Alonso, *Phys. Chem. Chem. Phys.*, 2016, **18**, 11885–11900.

30. W.-Y. Cha, T. Soya, T. Tanaka, H. Mori, Y. Hong, S. Lee, K. H. Park, A. Osuka and D. Kim, *Chem. Commun.*, 2016, **52**, 6076–6078.

31. N. Shivran, S. C. Gadekar and V. G. Anand, *Chem. – An Asian J.*, 2017, **12**, 6–20.

32. P. Shukla, M. D. Ambhore and V. G. Anand, *Chem. – A Eur. J.*, 2023, **29**, e202203327.

33. J. S. Park, *Abstr. 13th Int. Conf. Porphyrins Phthalocyanines (ICPP-13)*, 2024, p216.

34. P. Shukla, M. D. Ambhore and V. G. Anand, *Chem. Sci.*, 2024, **15**, 6022–6027.

35. G. Karthik, J. M. Lim, A. Srinivasan, C. H. Suresh, D. Kim and T. K. Chandrashekar, *Chem. – A Eur. J.*, 2013, **19**, 17011–17020.

36. S. Sahoo, P. Chatterjee, D. Blasco, D. Sundholm and H. Rath, *Org. Lett.*, 2024, **26**, 11045–11050.

View Article Online
DOI: 10.1039/D6SC00941G

37. T. Sarma, G. Kim, S. Sen, W.-Y. Cha, Z. Duan, M. D. Moore, V. M. Lynch, Z. Zhang, D. Kim and J. L. Sessler, *J. Am. Chem. Soc.*, 2018, **140**, 12111–12119.

38. H. S. Udaya and V. G. Anand, *Chem. – A Eur. J.*, 2024, **30**, e202403480.

39. X.-S. Ke, T. Kim, Q. He, V. M. Lynch, D. Kim and J. L. Sessler, *J. Am. Chem. Soc.*, 2018, **140**, 16455–16459.

40. V. Grover and M. Ravikanth, *Org. Lett.*, 2023, **25**, 4108–4112.

41. A. Srinivasan, V. M. Reddy, S. J. Narayanan, B. Sridevi, S. K. Pushpan, M. Ravikumar and T. K. Chandrashekar, *Angew. Chemie Int. Ed. English*, 1997, **36**, 2598–2601.

42. Y. Wei, B. Wang, W. Wang and J. Tian, *Tetrahedron Lett.*, 1995, **36**, 665–668.

43. N. S. Mills and K. B. Llagostera, *J. Org. Chem.*, 2007, **72**, 9163–9169.

44. D. Geuenich, K. Hess, F. Köhler and R. Herges, *Chem. Rev.*, 2005, **105**, 3758–3772.

45. M. Ishida, S. Karasawa, H. Uno, F. Tani and Y. Naruta, *Angew. Chemie Int. Ed.*, 2010, **49**, 5906–5909.

46. S. Fukuzumi, K. Ohkubo, M. Ishida, C. Preihs, B. Chen, W. T. Borden, D. Kim and J. L. Sessler, *J. Am. Chem. Soc.*, 2015, **137**, 9780–9783.

47. T. M. Krygowski and M. K. Cyrański, *Chem. Rev.*, 2001, **101**, 1385–1420.

48. (a) D. W. Szczepanik, M. Andrzejak, K. Dyduch, E. Żak, M. Makowski, G. Mazur and J. Mrozek, *Phys. Chem. Chem. Phys.*, 2014, **16**, 20514–20523. (b) D. W. Szczepanik, M. Andrzejak, J. Dominikowska, B. Pawełek, T. M. Krygowski, H. Szatylowicz and M. Solà, *Phys. Chem. Chem. Phys.*, 2017, **19**, 28970–28981.

49. J. L. Sessler, T. Morishima and V. Lynch, *Angew. Chemie Int. Ed. English*, 1991, **30**, 977–980.

50. D. Wu, A. B. Descalzo, F. Weik, F. Emmerling, Z. Shen, X.-Z. You and K. Rurack, *Angew. Chemie Int. Ed.*, 2008, **47**, 193–197.

View Article Online
DOI: 10.1039/D6SC00941G

51. T. Kubo, *Chem. Lett.*, 2015, **44**, 111–122.

52. (a) Z. Zeng, X. Shi, C. Chi, J. T. López Navarrete, J. Casado and J. Wu, *Chem. Soc. Rev.*, 2015, **44**, 6578–6596. (b) M. D. Ambhore, P. Shukla, R. G. Gonnade and V. G. Anand, *Chem. Commun.*, 2022, **58**, 8946–8949.

53. P. P. Desale, M.-S. Ko, T.-H. Roh, J.-I. Ham and D.-G. Cho, *J. Am. Chem. Soc.*, 2025, **147**, 480–487.

View Article Online
DOI: 10.1039/D6SC00941G

The data supporting this article has been included as part of the ESI. CCDC No. of **5:** 2432301